Atmospheric
Measurement
Techniques

Aerosol and cloud data processing and optical property retrieval algorithms for the spaceborne ACDL/DQ-1

Guangyao Dai[1], Songhua Wu[1,2,3], Wenrui Long[1], Jiqiao Liu[4], Yuan Xie[4], Kangwen Sun[1], Fanqian Meng[1], Xiaoquan Song[1,2], Zhongwei Huang[5], and Weibiao Chen[4]

[1]College of Marine Technology, Faculty of Information Science and Engineering,
Ocean University of China, Qingdao, 266100, China
[2]Laoshan Laboratory, Qingdao, 266200, China
[3]Institute for Advanced Ocean Study, Ocean University of China, Qingdao, 266100, China
[4]Key Laboratory of Space Laser Communication and Detection Technology, Shanghai Institute of Optics
and Fine Mechanics, Chinese Academy of Sciences, Shanghai, 201800, China
[5]Key Laboratory for Semi-Arid Climate Change of the Ministry of Education,
College of Atmospheric Sciences, Lanzhou University, Lanzhou, 730000, China

Correspondence: Songhua Wu (wush@ouc.edu.cn)

Abstract. The new-generation atmospheric environment monitoring satellite DQ-1, launched successfully in April 2022, carries the Aerosol and Carbon Detection Lidar (ACDL), which is capable of globally profiling aerosol and cloud optical properties with high accuracy. The ACDL/DQ-1 is a high-spectral-resolution lidar (HSRL) that separates molecular backscatter signals using an iodine filter and has 532 nm polarization detection and dual-wavelength detection at 532 and 1064 nm, which can be utilized to derive aerosol optical properties. The methods have been specifically developed for data processing and optical property retrieval according to the specific characteristics of the ACDL system and are introduced in detail in this paper. Considering the different signal characteristics and different background noise behaviors of each channel during daytime and nighttime, the procedures of data pre-processing, denoising process and quality control are applied to the original measurement signals. The aerosol and cloud optical property products of the ACDL/DQ-1, including the total depolarization ratio, backscatter coefficient, extinction coefficient, lidar ratio and color ratio, can be calculated by the retrieval algorithms presented in this paper. Two measurement cases with use of the ACDL/DQ-1 on 27 June 2022 and the global averaged aerosol optical depth (AOD) from 1 June to 4 August 2022 are provided and analyzed, demonstrating the measurement capability of the ACDL/DQ-1.

1 Introduction

Aerosols and clouds greatly affect the Earth's climate through their direct and indirect impact on the radiation budget. The altitude of the cloud layers and their multi-layer structures can influence the radiative balance of the Earth–atmosphere system by reflecting sunlight and absorbing and emitting thermal radiation. The aerosol radiative forcing significantly affects the atmospheric physical and chemical processes (Boucher et al., 2013). Therefore, as one of the largest uncertainties in global climate model, aerosols and clouds bring inaccuracy in estimating the climate change and weather forecasting (IPCC, 2014). Several studies show that local aerosol events also affect global climate change on a larger scale (IPCC, 2021; Dai et al., 2022). The satellite-based observations have great potential to acquire the global aerosols and clouds information. As a well-developed active remote sensing tool, lidars can provide aerosol and cloud profile measurements with high accuracy and high spatiotemporal resolution (King et al., 1999; Winker et al., 2007). The Cloud-Aerosol Lidar and Infrared Pathfinder Satellite Obser-

vation (CALIPSO) satellite was launched in April 2006, with a primary payload of the Cloud-Aerosol Lidar with Orthogonal Polarization (CALIOP) (Hunt et al., 2009). CALIOP produces a dataset of global vertically resolved cloud and aerosol properties, which gives inspiring insights into the understanding of the role of aerosols and clouds in the climate system (Winker et al., 2009). However, it is difficult to measure the lidar ratio with CALIOP as the Mie scattering and Rayleigh scattering are combined in the backscatter signal (Sayer et al., 2012). The lidar ratio is defined as the ratio of the aerosol extinction coefficient to the backscattering coefficient and is closely related to the physical and optical properties of the particles. The CALIOP team has developed the Hybrid Extinction Retrieval Algorithm (HERA), which retrieves both the particulate backscatter and extinction profiles from attenuated backscatter profile by including the scene classification (Young and Vaughan, 2009) as a priori data. By improving the algorithms for aerosol classification and lidar ratio selection, the accuracy of the inversion can be improved to some extent (Young et al., 2018). The previous validation studies have shown that a relatively large uncertainty would appear in extinction coefficient retrievals of aerosols and clouds as the lidar ratio is selected or modeled (Schuster et al., 2012; Balmes et al., 2019).

Taking advantage of the difference in spectral broadening, high-spectral-resolution lidar (HSRL) can separate the aerosol contribution from the molecular backscatter with a narrow bandwidth optical filter (Fiocco and DeWolf, 1968; Shimizu et al., 1983). Thus, without assuming the lidar ratio, the aerosol backscatter and extinction coefficients can be obtained simultaneously. HSRL uses several techniques to achieve a clear separation between Mie and Rayleigh scattering spectra, including the Fabry–Pérot interferometer edge technique approach (Garnier and Chanin, 1992; Flesia and Korb, 1999), interferometric fringe imaging techniques (Matthew and James, 1998), and atomic or molecular filter discrimination (She et al., 1992; Liu et al., 1997). Many HSRL instruments have been successfully implemented to measure the atmospheric parameters or particle optical properties by means of ground-based lidars and airborne lidars (Esselborn et al., 2008; Li et al., 2008; Müller et al., 2014). The Aeolus satellite, which carries a Fabry–Pérot-interferometer-based wind lidar (Atmospheric LAser Doppler Instrument, ALADIN), was successfully launched in 2018. It could provide the atmospheric optical properties by independently measuring the particle extinction coefficients, the co-polarized particle backscatter coefficients and the co-polarized lidar ratio by the standard correct algorithm (SCA) (Flamant et al., 2008; Flamant et al., 2021). Additionally, Aeolus optimizes the aerosol optical properties using a maximum likelihood estimation, due to the noise sensitivity of the SCA as an algebraic inversion scheme (Ehlers et al., 2022). The Earth Clouds, Aerosols and Radiation Explorer (EarthCARE), which deploys a HSRL atmospheric lidar (ATLID) (Illingworth et al., 2015; Eisinger et al., 2023;

Wandinger et al., 2023), is scheduled to be launched in 2024 (Wehr et al., 2023).

The Chinese atmospheric environment monitoring satellite DQ-1 was successfully launched for the first time on 16 April 2022. As an integrated detection scientific research satellite, it will serve as an important part of the Chinese atmospheric environment monitoring system. The DQ-1 is operated in a sun-synchronous orbit at the altitude of 705 km and provides global comprehensive monitoring of atmospheric particles, carbon dioxide (CO_2), aerosols and clouds. For the combination of the active and passive measurements, the DQ-1 is equipped with five sensors including the Aerosol and Carbon Detection Lidar (ACDL), the Particulate Observing Scanning Polarimeter (POSP), the Directional Polarization Camera (DPC), the Environmental trace gas Monitoring Instrument (EMI) and the Wide Swath Imaging system (WSI). The primary payload carried by the DQ-1 is the ACDL, which is a lidar system consisting of two different modules. The first is the aerosol-measurement module which provides aerosol and cloud profile measurements with high accuracy globally, and the second is the CO_2-measurement module for atmospheric column CO_2 observations (Chen et al., 2023). In previous studies, the ACDL scientific team measured the transmittance of the different absorption lines under different temperatures of the iodine wall and finger (Dong et al., 2018). The reliability of the spaceborne system was confirmed through simulation and performance evaluation (Liu et al., 2019; Yu et al., 2018), and the impact of errors was also assessed (Zhang et al., 2018). Finally, the algorithmic and theoretical foundation of the spaceborne HSRL loaded on DQ-1 is established. The airborne ACDL prototype (A2P) was developed and mounted on an airplane to conduct the calibration and validation experiments over Qinhuangdao, China, in March 2019. The spatial and temporal developments of the atmospheric boundary layer (ABL) and aerosol distribution along the flight routes were obtained in this experiment (Wang et al., 2020; Ke et al., 2022).

In this paper, the ACDL Aerosol module (ACDL-A) measurement principles are introduced. The retrieval methods applied for the aerosol optical property calculation are presented. Finally, two long-term global aerosol optical property distribution measurement cases are provided. In this work, a data pre-processing process is designed that fits the characteristics of ACDL laser transmitting, receiving and data acquisition. The data quality control and segmentation denoising algorithms used in data processing show considerable noise suppression capabilities.

The paper is organized as follows. Section 2 describes the composition and working principle of the ACDL-A. Sections 3 and 4 contain the detailed description of the data processing and the optical properties retrieval algorithms. In Sect. 5 we provide two measurement cases of optical parameter products and 2 months of global observations in order to demonstrate the capabilities of the presented algorithms. Conclusions and prospects are summarized in Sect. 6.
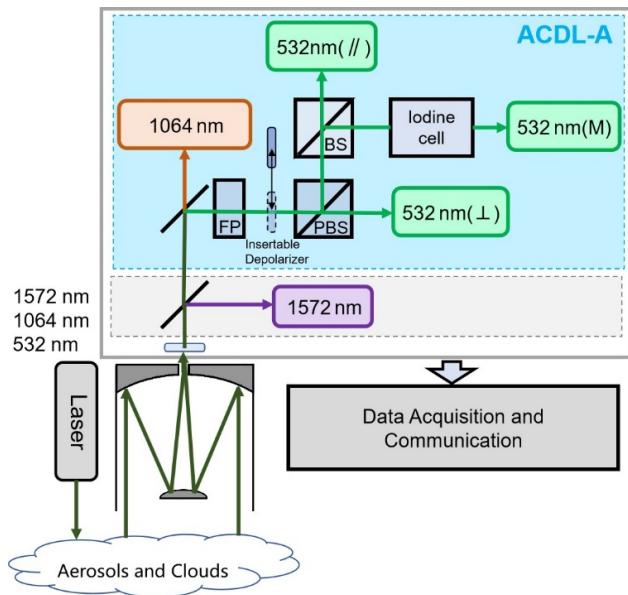
Figure 1. Schematic diagram of ACDL-A.

2 Overview of the ACDL-A

The ACDL consists of a transmitter for generating the laser pulses down through the atmosphere, a receiver for collecting the backscatter lights from the atmospheric particles, a detection and data acquisition that measures signal strength and prepares for data downlink. The functional description of ACDL is provided in Fig. 1. The transmitter contains a three-wavelength laser which emits laser beams at the wavelengths of 532, 1064 and 1572 nm. The output pulse energies at each wavelength are monitored by energy meters. With the repetition frequency of 20 Hz, the laser emits two pulses successively with a time interval of 200 μs. This configuration of the laser emission strategy, which is called dual pulse, has a horizontal resolution of 337 m on the surface for the original profile. Because of the dual-pulse design, we present a practical data process, which is described in detail in Sect. 3.

The ACDL takes advantage of the low transmittance valley of the iodine vapor absorption filter at 1110 line to block Mie scattering with a narrow spread. Meanwhile, the broader Rayleigh scattering can pass through (Liu et al., 1997). As shown in Fig. 1, the backscatter lights are divided into 532 nm channels (including cross-polarized and parallel-polarized channels and high-spectral-resolution channel) and 1064 nm channel in the spectroscopic module. The cross-polarized and parallel-polarized channels at 532 nm are designed for the measurements of the linear particle depolarization ratio. After being reflected by the polarization beam splitter (PBS), the lights are split again by a beam splitter (BS), and a portion of the parallel-polarized signal passes through the iodine absorption filter, thus constituting the molecular channel to estimate the optical properties of

aerosol particles and clouds. Additionally, the 1064 nm channel adopts the same sampling frequency as 532 nm channels for atmospheric detection in the ACDL-A.

To facilitate the distinction of the parameters of each channel, the 1064 nm channel is denoted with the subscript "1064", while the 532 nm channels are not specifically marked with the wavelength subscript. The superscripts of $\|$, $\perp$ and M are used to represent the parallel-polarized channel, cross-polarized channel and high-spectral-resolution channel at 532 nm, respectively. The signal intensity of these four channels in the ACDL-A module can be expressed using the lidar equations as follows:

$$P^{\|}(z,\lambda) = E\frac{C^{\|}K^{\|}}{(z-z_0)^2}\left[\beta_{\mathrm{m}}^{\|}(z,\lambda) + \beta_{\mathrm{a}}^{\|}(z,\lambda)\right]T^2(z,\lambda), \quad (1)$$

$$P^{\perp}(z,\lambda) = E\frac{C^{\perp}K^{\perp}}{(z-z_0)^2}\left[\beta_{\mathrm{m}}^{\perp}(z,\lambda) + \beta_{\mathrm{a}}^{\perp}(z,\lambda)\right]T^2(z,\lambda), \quad (2)$$

$$P^{M}(z,\lambda) = E\frac{C^{M}K^{M}}{(z-z_0)^2}\left[f_{\mathrm{m}}\beta_{\mathrm{m}}^{M}(z,\lambda) + f_{\mathrm{a}}\beta_{\mathrm{a}}^{M}(z,\lambda)\right]T^2(z,\lambda) \quad (3)$$

and

$$P(z,\lambda_{1064}) = E_{1064}\frac{C_{1064}K_{1064}}{(z-z_0)^2}[\beta_{\mathrm{m}}(z,\lambda_{1064}) + \beta_{\mathrm{a}}(z,\lambda_{1064})]T^2(z,\lambda_{1064}), \quad (4)$$

where $P(z,\lambda)$ is the measured power at the height of z received by the channel with the wavelength of λ, E is the single pulse energy, and C and K represent the calibration constants and the system constants containing optical efficiency and gain coefficients. It is to be pointed out that in the data processing work in this paper, all heights are standardized to the orthometric height, where z is the altitude to the local geodetic level. $(z-z_0)$ is the distance between the altitude where the detected particle is located and the satellite altitude. β denotes the backscatter coefficient at z with a certain wavelength and uses the subscripts m and a to represent the molecule and particle (aerosols and clouds). And T^2 is the round-trip transmittance between observation area z and z_0. The transmittance of iodine filter for molecular scattering is denoted by f_{m}, which is a function of height due to its dependence on atmospheric temperature and pressure. And the transmittance of iodine filter for aerosol scattering is denoted by f_{a}.

The molecular backscattering coefficient β_{m} and the molecular extinction coefficient α_{m} can be calculated according to the Rayleigh scattering theory (Bodhaine et al., 1999; Collis and Russell, 1976), and the inversion of the aerosol optical parameters can be achieved by combining the above equations (Hair et al., 2008; Liu et al., 2013).

3 ACDL-A data preparation

As shown in Fig. 2, the ACDL-A data processing procedure consists of data preparation, pre-processing and optical prop-

Table 1. Parameters of the ACDL instrument.

Parameters	Value
Wavelength	532.024 nm; 1064.490 nm
Pulse energy	~ 130 mJ at 532 nm; ~ 180 mJ at 1064 nm
Laser frequency stability	< 2 MHz (RMS)
Laser divergence angle	≤ 60 µrad at 532/1064 nm
Gain	59.46 at parallel; 53.4573 at vertical; 32 at HSRL
Telescope diameter	1.0 m
Lidar off-nadir angle	2°
Laser repetition frequency	20 Hz at dual-pulse
Sampling rate	50 MHz
Vertical resolution (raw data)	3 m at < 7.5 km; 24 m (8 bin average) at > 7.5 km
Horizontal resolution (raw data)	~ 330 m
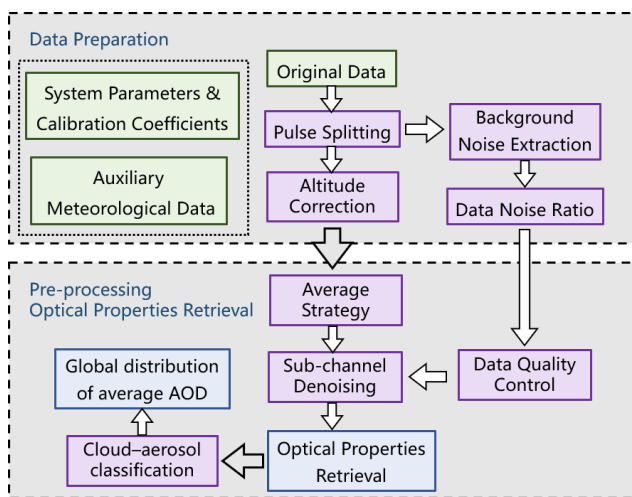
Figure 2. Flowchart of the ACDL-A data process. The green box represents the input data, the purple box shows the data processing step, and the blue part indicates the output data products.

erties retrieval. This section describes the data preparation of removing the background noise from the original voltage signal returned through the sub-channel and correcting its elevation. Additionally, the auxiliary data prepared for the inversion algorithm are also introduced in this section.

3.1 Dual-pulse data processing

The laser in the ACDL-A transmitter applies a unique dual-pulse emission configuration, which emits a pair of pulses continuously with a repetition frequency of 20 Hz. In other words, the laser emits a total of 40 pulses in 1 s, where every pair of pulses are grouped together, and the first pulse (odd pulse) is launched 200 µs before the second pulse (even pulse). As shown in Fig. 3, after triggering a set of dual pulses, the blue line at 16.1 µs is the duration of odd-pulse emission, and the orange line is the even-pulse emission duration. The time between the emission of the odd pulse (the

blue line) and the start of signal acquisition (the dashed blue line) is referred to as the "time delay". After completing the full height data acquisition of the odd pulse, the backscatter signals stimulated by the even pulse are acquired immediately afterwards. Since all the channels of ACDL-A are sampled with a frequency of 50 MHz in the data acquisition module, the corresponding fundamental vertical spatial resolution is 3 m. To improve the satellite data downlink transfer efficiency, as shown in Fig. 3, the original data are 8-bin-averaged at high altitude.

Since the original signal contains two pulses with different height resolution data, it is necessary to match odd pulses and even pulses in altitude separately in the data preparation phase. Based on the time of emission and acquisition, the position of each data point relative to the satellite can be calculated. The latitude and longitude of the laser footprint points corresponding to each set of dual pulses were determined using spacecraft attitude and ephemeris data. The ellipsoidal heights corresponding to each data point of the odd pulses and even pulses are calculated separately by the WGS-84 (Lohmar, 1988) coordinate system and then converted to orthometric height using the geoid height. For certain vertical resolution requirements in subsequent processing, the odd and even pulses will be averaged bin by bin by matching them to the appropriate height interval.

3.2 Sub-channel background denoising

In previous studies, the background noise was usually removed by subtracting the mean values of the "signals" at high altitude during the data processing of satellite-based lidars (Luthcke et al., 2021; Kar et al., 2018). The high-altitude signals are selected because then only the background noise due to the solar and dark counts from detectors is included in the signals. Due to the special data acquisition strategy of the dual-pulse configuration, the maximum observation altitude of the odd pulse can be higher than 40 km (maximum detection altitude is jointed determined by the latitude and elevation). As shown in Fig. 3, after completing the sig-
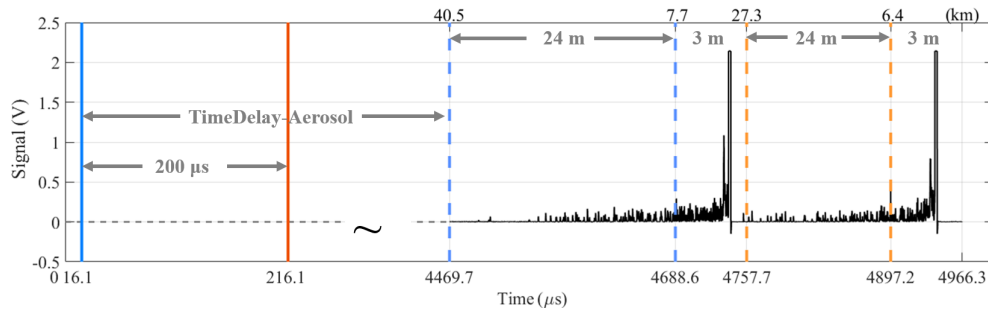
Figure 3. Timing diagram for dual-pulse emission and acquisition.

nal acquisition of odd pulses, the maximum observation altitude collected for the even pulse is about 27 km. Hence the signal of the odd pulse is selected for background noise extraction in each channel. To avoid the effect of possible aerosol layers at high altitude, the minimum values of the segmented-averaged signal in the parallel-polarized channel and cross-polarized channel of 532 nm are selected as background noise, while the signals at high altitude are removed as background noise in the high-spectral-resolution channel and 1064 nm channel.

The amplitude of background signal in each channel is closely related to the observed location and time period. Figure 4 (a1) to (a4) and (b1) to (b4) show the background signal extracted from each channel during nighttime and daytime, respectively. The background signal of the 532 nm parallel-polarization channel is relatively stable and varies from 0.002 to 0.005 V during nighttime. During daytime, due to the different irradiance at different locations and underlying surfaces, the background signal fluctuates at the range of 0.002 to 0.5 V. The background signal of cross-polarized channel and high-spectral-resolution channel manifest similar characteristics. The cross-polarized channel background signal level at nighttime is more stable at around 0.005 V, while it is more sensitive and even reaches 1.5 V at daytime. The high-spectral-resolution channel background signal is normally below 0.002 V at nighttime and is increased obviously during the daytime. The aerosol backscatter signal from the 1064 nm channel is slightly affected by sunlight. The fluctuations in the value of the daytime background signal are related to the intensity of solar radiation at different latitudes, solar energetic events, feature type, and cloud albedo. The high values of the initial sets of nighttime observations in Fig. 4a1 to a3 may result from the remaining solar radiation at dusk.

3.3 Auxiliary dataset preparation

The auxiliary datasets contain the system parameters and meteorological data. The system parameters C and K for each channel are provided by the ACDL scientific team, which will be not discussed in this paper. The main meteorological datasets required in the inversion algorithms include
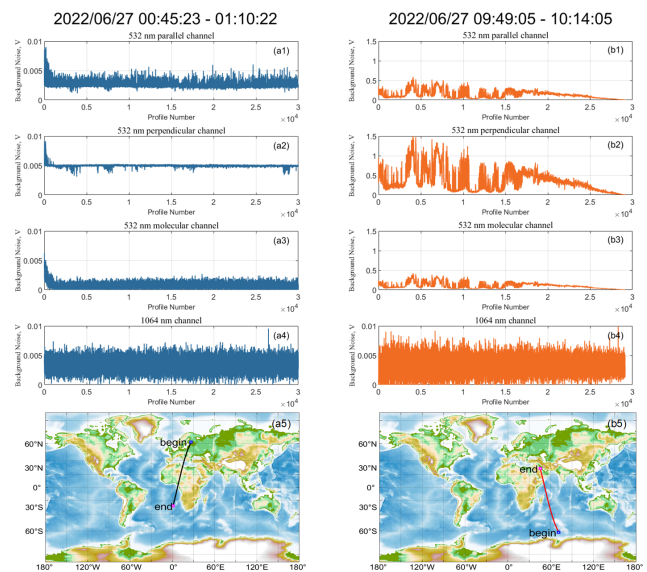

Figure 4. The background signal value subtracted from each echo signal in nighttime (blue line on the left) or daytime (orange line on the right) segment of data, both on 27 June 2022. Corresponding to each channel in order from top to bottom, **(a1, b1)** parallel-polarized channel at 532 nm, **(a2, b2)** cross-polarized channel at 532 nm, **(a3, b3)** molecular channel at 532 nm, **(a4, b4)** 1064 nm channel and **(a5, b5)** satellite orbit.

the atmospheric temperature and pressure. The calculation of the transmittance of iodine filter for molecular scattering f_{m} is highly reliant on them. The global temperature, ozone mass mixing ratio and pressure data are collected from the European Centre for Medium-Range Weather Forecasts (ECMWF) fifth-generation reanalysis (ERA5) dataset (Hersbach et al., 2023). The ERA5 data provide hourly averaged global atmospheric parameters, with a 0.25° latitude ×0.25° longitude resolution grid with 37 pressure levels. The ERA5 global data are matched according to the latitude and longitude of the ACDL-A, and the pressure gradient data are then matched to the corresponding altitude of the lidar signal using cubic spline interpolation.
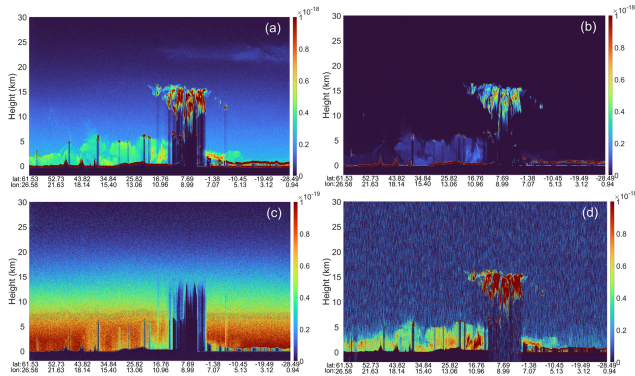
Figure 5. ACDL-A optical power signals in **(a)** the 532 nm parallel polarized channel, **(b)** the 532 nm perpendicular polarized channel, **(c)** the 532 nm molecular channel and **(d)** the 1064 nm channel on 00:45:23 to 01:10:22 UTC on 27 June 2022.

4 Retrieval algorithms

4.1 Pre-processing

4.1.1 Average strategy and quality control

To improve the signal quality and reduce the interference of transient clutter, the raw data in each channel are averaged vertically and horizontally. After the assessments of different averaging scales, a vertical averaging scale of 50 m and horizontal averaging scale of 3.3 km (10 pairs of dual pulses) for nighttime data are chosen in this work. Considering that the solar background radiation at daytime causes a lower signal-to-noise ratio and more noise clutter, a wider range of averaging scale is applied during daytime. The daytime measurement data from high-spectral-resolution channel are averaged with the vertical scale of 50 m and horizontal scale of 10 km (30 pairs of dual pulses). Figure 5 shows that after implementing the averaging strategy described above, the optical power signals for each channel are calculated using the system parameters and monthly calibration coefficients.

From Fig. 5, the cloud layers at about 6–16 km and aerosol layers within the atmospheric boundary layer are observed in the parallel-polarized channel and cross-polarized channel after pre-processing procedure. However, the high-altitude aerosol layer at about 25 km is only captured by the parallel-polarized channel with a faint signal, showing weak depolarization characteristics. The molecular channel has signal intensity that is an order of magnitude lower than the other channels, making it more susceptible to noise, as shown in the Fig. 5c, which shows the presence of scattering noise. Hence it is more crucial to denoise the high-spectral-resolution channel signals in the subsequent retrieval algorithms. The 1064 nm band almost has no response to molecular backscattering, and its optical power signal with low aerosols and clouds content behaves as a weakly fluctuating noise.
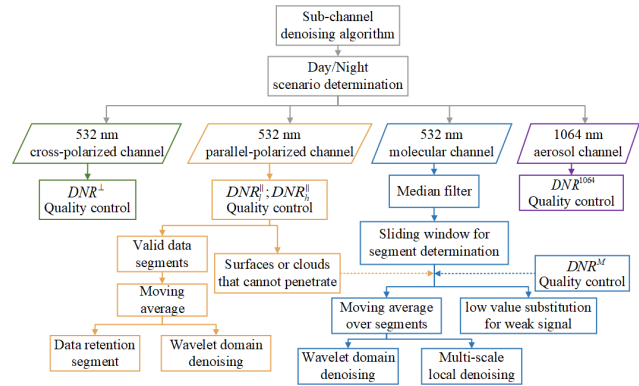

Figure 6. Flowchart of the ACDL-A sub-channel denoising algorithms.

To evaluate the single channel echo signal quality, a parameter named data-to-noise ratio (DNR) is introduced to calculate the ratio of the signal and subtracted background noise P_{noise} at a certain height. The DNR is calculated by Eq. (5):

$$\mathrm{DNR}\,(z,\lambda) = \frac{P\,(z,\lambda) + P_{\mathrm{noise}}}{P_{\mathrm{noise}}}. \tag{5}$$

The DNR can be used for the data quality control by setting reasonable thresholds for daytime–nighttime scenarios for each channel. It will serve as the segmentation basis for the high-spectral-resolution channel denoising algorithm in the following subsection.

4.1.2 Sub-channel denoising algorithm

After completing the signal averaging process described in the previous sections, the noise still prevents the inversion of the optical parameters for the HSRL method. Due to the different optical path designs of channels in the ACDL, the signal characteristics behave distinctly. In this work, a set of sub-channels denoising algorithms is designed especially for each channel as shown in Fig. 6. The target of the denoising algorithm is to preserve the useful information as much as possible from the optical signal data, to remove the high-frequency noise and outliers, and to obtain smoother data profiles.

After the data averaging procedure, different thresholds are chosen for each channel based on the day–night flag in the auxiliary data segment of ACDL-A. Distinct aerosol and cloud layers can be observed in the 532 nm cross-polarized channel and 1064 nm channel echo signals. The desired signal can be extracted from the overall echo profiles using a suitable threshold in the corresponding $\mathrm{DNR}^{\perp}$ and DNR^{1064} profiles. The parallel-polarized channel signal is divided into three parts using $\mathrm{DNR}^{\|}$ thresholds. The valid data segments are subjected to a four-point sliding average, and the aerosol and cloud layers with high data quality are extracted as a "data retention segment" using thresholds, pre-
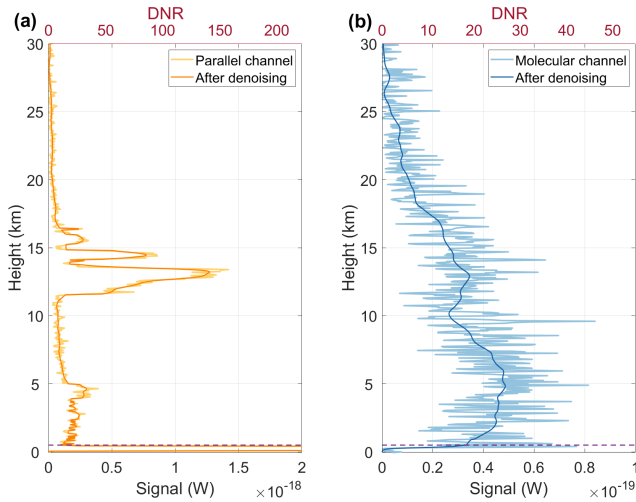
Figure 7. 532 nm parallel polarized channel (a) and molecular channel (b) denoised profiles, the light color line is the original signal, the dark color line is after denoising.

serving as much of the original signal variation as possible. The remaining valid data segments of this profile then undergo "sym4" wavelet denoising (Daubechies, 1988; Fang and Huang, 2004), as shown in Fig. 6. The echo signal is rapidly saturated at thick clouds that cannot be penetrated or at Earth's surface, and height position (such as the purple dashed line in Fig. 7) is localized in the corresponding high-spectral-resolution channel signal. To ensure spatial continuity of the observed profiles, a 2-D median filter is applied to the molecular channel signals of the entire orbit using a 5×3 window (250 m vertically $\times 6.6$ km horizontally). Next, it extracts low-quality signals in the high-altitude, subsurface and totally attenuated regions based on the DNR thresholds and corresponding parallel channel segmentation position, using a 20-point sliding window. The sliding window method ensures that occasional spikes in the signal do not interrupt the continuity of data segmentation. To maintain the continuity of subsequent data processing, low-quality signals are not eliminated but uniformly labeled as low values. The valid detection segments of the molecular channel are subject to a maximum of 20 points of slide averaging, depending on their length. Wavelet denoising and multiscale local 1-D polynomial transform are used for further denoising, with the overall goal of obtaining a smoother profile that can represent the trend of the signal.

The signals of each channel after segmentation and denoising are re-spliced according to the height in a way that maintains local continuity. After the data pre-processing has been completed, the DNR is still used in subsequent inversion algorithms to represent the quality of the data.

4.1.3 Optical property retrieval

The aerosol and cloud optical property products of ACDL/DQ-1 include the total depolarization ratio, backscatter coefficient, extinction coefficient, lidar ratio and color ratio.

The total depolarization ratio $\delta(z)$ is the ratio of total backscattering coefficient in the vertical polarization direction to that in the parallel polarization direction, which is used to describe the shape characteristics of the aerosol particles and is related to the degree of regularity of the particle shape. The total depolarization ratio can be calculated via

$$\delta(z) = \frac{\beta_m^{\perp}(z) + \beta_a^{\perp}(z)}{\beta_m^{\parallel}(z) + \beta_a^{\parallel}(z)} = \frac{P^{\perp}(z,\lambda)\,C^{\parallel}K^{\parallel}}{P^{\parallel}(z,\lambda)\,C^{\perp}K^{\perp}}. \tag{6}$$

With the high-spectral-resolution channel, the ACDL-A enables direct detection of aerosol backscattering coefficient $\beta_a(z)$ and extinction coefficient $\alpha_a(z)$ by associating Eqs. (1)–(3), which are expressed as

$$\beta_a(z) = \beta_m(z)\frac{[1+\delta(z)]\,[f_m(z) - f_a]\,R(z)}{(1+\delta_m)\,[1 - f_a R(z)]}$$
$$- \beta_m(z) \quad \text{and} \tag{7}$$

$$\alpha_a(z) = \frac{\partial \tau(z)}{\partial z} - \alpha_m(z). \tag{8}$$

The temperature and pressure profiles modeled with ERA5 are used to obtain the molecular scattering spectra at each height through the atmospheric model (Tenti et al., 1974; Shneider et al., 2004; Gu et al., 2013) and to calculate the $f_m(z)$ and $\alpha_m(z)$. The δ_m represents the molecular depolarization ratio, which can be also affected by the interference filter specifications and is usually set as a constant. The $R(z)$ is the backscattering ratio of 532 nm parallel channel signal to the high-spectral-resolution channel signal.

The atmospheric aerosol optical depth (AOD) is defined as the integral of the aerosol extinction coefficient and molecular extinction coefficient over all heights. Conversely the gradient of AOD over height can be used to calculate α_a. And the $\tau(z)$ can be calculated from the transmittance as in Eq. (9):

$$\tau(z) = -\frac{1}{2}\ln\left[T^2(z,\lambda)\right]. \tag{9}$$

The multiple scattering of clouds is considered in this algorithm, where division by the multiple scattering factor η represents the required correction of the measured transmittance (Hu, 2007; Garnier et al., 2015).

The magnitude of aerosol lidar ratio $S_a(z)$ is influenced by the aerosol absorption and scattering characteristics and is one important parameter to distinguish the aerosol types. As shown in Eq. (10), it is calculated as the ratio of the aerosol

extinction coefficient to the backscattering coefficient:

$$S_a(z) = \frac{\alpha_a(z)}{\beta_a(z)}. \quad (10)$$

The ACDL-A has a dual-wavelength observation capability of obtaining the attenuated color ratio $\chi'(z)$, which is defined as the ratio of the attenuated backscatter coefficient $B_\lambda(z)$ at 1064 nm to that at 532 nm, where $B_\lambda(z)$ has been calibrated by the ozone and molecular two-way transmittance through the atmosphere (Vaughan et al., 2019):

$$\chi'(z) = \frac{B_{1064}(z)}{B_{532}(z)} \quad . \quad (11)$$

In this algorithm, the gradient calculation on AOD profiles amplifies the noise effect from the high-spectral-resolution channel. Although the sub-channel denoising algorithm has been deployed to remove the noise, the uncertainties in the low-quality signal remain.

5   Results and discussion

The size of each segment is limited when ACDL-A data is transmitted back through the satellite transceiver system, and each track datum is divided into two views by day and night, and each view contains two segments for subsequent data processing. Figure 8 presents the aerosol optical properties of two segments of ACDL observations at middle–low latitudes on 27 June 2022.

Figure 8 (a1) to (e1) present the retrieval results with high data quality during nighttime. In the eastern European urban agglomeration (area <I>), the total depolarization ratios are 0.08 ± 0.02, and lidar ratios at 532 nm are 50 ± 20 sr, thus indicating that the urban pollution aerosols may dominate within the boundary layer in this area (Burton et al., 2012). The satellite flew over the Sahara with the footprint cross area <II>. The dominant aerosol type changes from urban pollution aerosols to mixed dust, with a total depolarization ratio of 0.32 ± 0.03, aerosol lidar ratio of 39 ± 12 sr and higher extinction coefficient than that within area <I>. In area <III>, some clouds that existed at the range of 6 and 16 km can be observed over the Atlantic Ocean in the Southern Hemisphere. There are structural features of the aerosol layers in the vertical and horizontal directions as seen in the optical properties of each area, which are often assumed to be a single-type aerosol with the same optical characteristics in the absence of HSRL detection capabilities. As shown in area <V> of Fig. 8b1, a thin aerosol layer exists at altitudes of 22–26 km, mainly confined between 15° N and 28° S. This layer of aerosols is likely to be smoke or sulfate from the January 2022 Tonga eruption (Legras et al., 2022). Due to the low signal strength of this layer, observations are only available in the 532 nm aerosol backscatter coefficient with the current version algorithm.
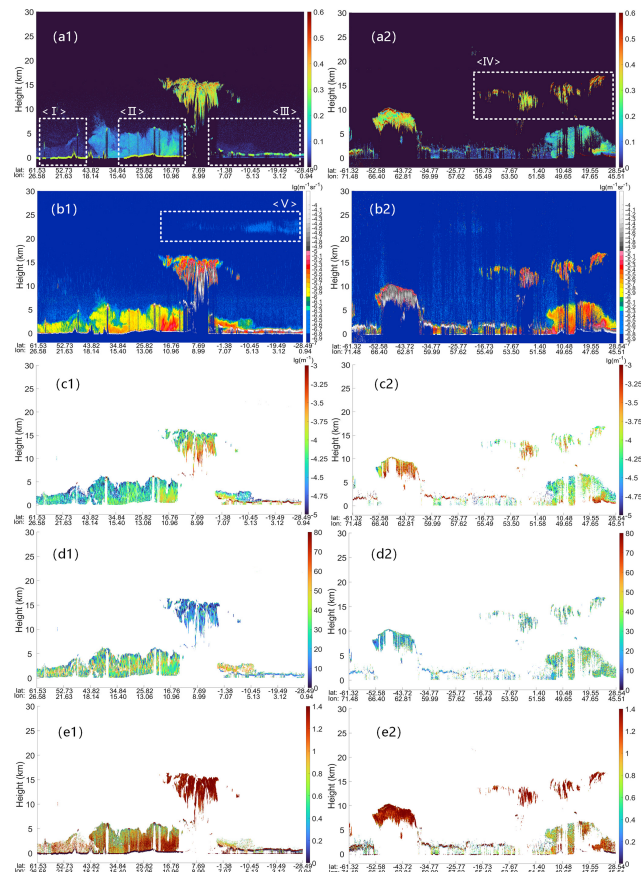

Figure 8. Retrievals from ACDL-A measurements between 00:45:23 and 01:10:22 (nighttime, **a1–e1**) and between 09:49:05 and 10:14:05 (daytime, **a2–e2**) on 27 June 2022. From top to bottom: the time series of **(a1, a2)** the total depolarization ratio, **(b1, b2)** the backscattering coefficient, **(c1, c2)** the extinction coefficient, **(d1, d2)** the lidar ratio and **(e1, e2)** the attenuated color ratio.

The daytime observations of aerosols and clouds by ACDL are influenced by solar light; thus they have lower quality compared to the measurement data during nighttime, as shown in Fig. 8a2 to e2, which are from a segment of data that crosses from the Indian Ocean to the Arabian Peninsula. The ACDL receives a stronger signal from solar background radiation during daylight hours, causing saturation of the detector and faster attenuation of the effective signal when cloud cover is encountered. As shown in area <IV>, the aerosol layers below the clouds cannot be distinguished from the noise.

The algorithms for processing and retrieval are appropriate for batch operations of ACDL data under various conditions, including daytime and nighttime, different features, and different area. The data production processing rate can meet the satellite data processing needs after proper optimization. As shown in Fig. 9a, the total column AOD (Pan et al., 2022) is calculated with the aerosol optical parameters retrieved from ACDL-A data from 1 June to 4 August 2022. The aerosol
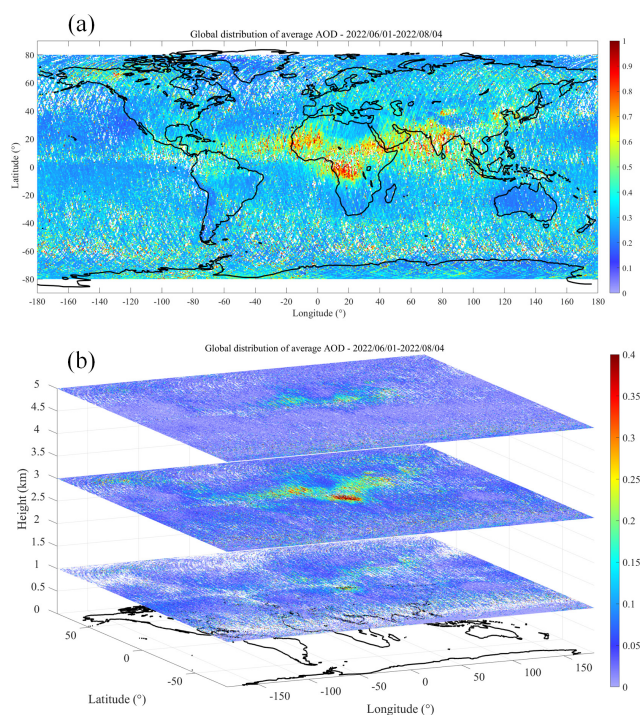
Figure 9. (a) Global averaged AOD for 1 June to 4 August 2022. **(b)** Slices of the global distribution of AOD at different height range from 1 June to 4 August 2022.

profile data are quality-screened; most clouds are removed by setting thresholds for the optical properties and then aggregated onto a global $0.25° \times 0.25°$ latitude-longitude grid. The global AOD describes the attenuation of light by aerosols and is an important indicator reflecting the degree of air pollution (Levy et al., 2013), The AOD at different heights can also be obtained with ACDL-A. In Fig. 9b, the slice diagrams show the global distribution of the layer average AOD in the three height ranges of surface–1, 1–3, and 3–5 km, respectively.

6   Summary and outlook

This paper gives an overview of the main algorithms applied to derive the aerosols and clouds optical properties product of ACDL/DQ-1. ACDL brings a major advance in spaceborne active remote sensing of aerosols and clouds. The ACDL-A data processing algorithms have unique aspects designed to take advantage of these new capabilities. The ACDL-A data processing procedure consists of data preparation, pre-processing and optical property retrieval. Based on the unique dual-pulse emission configuration and averaging strategy, the algorithm can deliver data products with a horizontal resolution of 3.3 km and a vertical resolution of 50 m. Pre-processing algorithms have been developed for the data characteristics of each channel, and data quality control schemes have been designed for both day and night

scenarios, after background signals have been removed. In view of the data characteristics of different channels, a set of sub-channels denoising algorithms are designed specifically for each channel. The capacity of the ACDL-A to independently measure backscatter coefficient and extinction coefficient is also demonstrated by two observation cases on 27 June 2022, where the retrieved lidar ratio is calculated as well. The data processing and retrieval algorithms are applied to the long-term ACDL/DQ-1 observation campaign, and a measurement case of the average AOD global distribution is provided.

The ACDL scientific team is gradually accumulating the datasets of optical products as observations in orbit proceed, and related validation activities are ongoing. Although the retrieval of the aerosol optical properties can be realized stably, the algorithms still need to be optimized further. The experience gained from analyzing the data acquired by ACDL has led to many improvements, with significant room for optimization on low-quality data and noise control. Various further algorithm improvement efforts are ongoing. Additionally, the ACDL scientific team is developing a unique scene classification algorithm based on the aerosol and cloud optics products, which requires additional improvement of the algorithms for optical property retrieval.

Review statement. This paper was edited by Ulla Wandinger and reviewed by two anonymous referees.

References

Balmes, K. A., Fu, Q., and Thorsen, T. J.: Differences in Ice Cloud Optical Depth From CALIPSO and Ground-Based Raman Lidar at the ARM SGP and TWP Sites, J. Geophys. Res.-Atmos., 124, 1755–1778, https://doi.org/10.1029/2018JD028321, 2019.

Boucher, O., Randall, D., Artaxo, P., Bretherton, C., Feingold, G., Forster, P., Kerminen, V.-M., Kondo, Y., Liao, H., Lohmann, U., Rasch, P., Satheesh, S. K., Sherwood, S., Stevens, B., and Zhang, X. Y.: Clouds and aerosols. Climate Change 2013: The Physical Science Basis, edited by: Stocker, T.F., Qin, D., Plattner, G.-K., Tignor, M., Allen, S. K., Boschung, J., Nauels, A., Xia, Y., Bex, V., and Midgley, P. M., Cambridge University Press, 571–658, https://doi.org/10.1017/CBO9781107415324.016, 2014.

Bodhaine, B. A., Wood, N. B., Dutton, E. G., and Slusser, J. R.: On Rayleigh Optical Depth Calculations, J. Atmos. Ocean. Technol., 16, 1854–1861, 1999.

Burton, S. P., Ferrare, R. A., Hostetler, C. A., Hair, J. W., Rogers, R. R., Obland, M. D., Butler, C. F., Cook, A. L., Harper, D. B., and Froyd, K. D.: Aerosol classification using airborne High Spectral Resolution Lidar measurements – methodology and examples, Atmos. Meas. Tech., 5, 73–98, https://doi.org/10.5194/amt-5-73-2012, 2012.

Chen, W., Liu, J., Hou, X., Zang, H., Ma, X., Wan, Y., and Zhu, X.: Lidar Technology for Atmosphere Environment Monitoring Satellite, Aerospace Shanghai (in Chinese and English), 3, 13–20,110, https://doi.org/10.19328/j.cnki.2096-8655.2023.03.002, 2023.

Collis, R. T. H. and Russell, P. B.: Lidar measurement of particles and gases by elastic backscattering and differential absorption, in: Laser Monitoring of the Atmosphere, edited by: Hinkley, E. D., Springer Berlin Heidelberg, 71–151, https://doi.org/10.1007/3-540-07743-X_18, 1976.

Dai, G., Sun, K., Wang, X., Wu, S., E, X., Liu, Q., and Liu, B.: Dust transport and advection measurement with spaceborne lidars ALADIN and CALIOP and model reanalysis data, Atmos. Chem. Phys., 22, 7975–7993, https://doi.org/10.5194/acp-22-7975-2022, 2022.

Daubechies, I.: Orthonormal bases of compactly supported wavelets, Commun. Pure Appl. Math., 41, 909–996, https://doi.org/10.1002/cpa.3160410705, 1988.

Dong, J., Liu, J., Bi, D., Ma, X., Zhu, X., Zhu, X., and Chen, W.: Optimal iodine absorption line applied for spaceborne high spectral resolution lidar, Appl. Opt., 57, 5413–5419, https://doi.org/10.1364/AO.57.005413, 2018.

Ehlers, F., Flament, T., Dabas, A., Trapon, D., Lacour, A., Baars, H., and Straume-Lindner, A. G.: Optimization of Aeolus' aerosol optical properties by maximum-likelihood estimation, Atmos. Meas. Tech., 15, 185–203, https://doi.org/10.5194/amt-15-185-2022, 2022.

Eisinger, M., Marnas, F., Wallace, K., Kubota, T., Tomiyama, N., Ohno, Y., Tanaka, T., Tomita, E., Wehr, T., and Bernaerts, D.: The EarthCARE Mission: Science Data Processing Chain Overview, EGUsphere [preprint], https://doi.org/10.5194/egusphere-2023-1998, 2023.

Esselborn, M., Wirth, M., Fix, A., Tesche, M., and Ehret, G.: Airborne high spectral resolution lidar for measuring aerosol extinction and backscatter coefficients, Appl. Opt., 47, 346–358, https://doi.org/10.1364/AO.47.000346, 2008.

Fang, H. and Huang, D.: Noise reduction in lidar signal based on discrete wavelet transform, Opt. Commun., 233, 67–76, https://doi.org/10.1016/j.optcom.2004.01.017, 2004.

Fiocco, G. and DeWolf, J. B.: Frequency Spectrum of Laser Echoes from Atmospheric Constituents and Determination of the Aerosol Content of Air, J. Atmos. Sci., 25, 488–496, https://doi.org/10.1175/1520-0469(1968)025<0488:FSOLEF>2.0.CO;2, 1968.

Flamant, P., Cuesta, J., Denneulin, M., Dabas, A., and Huber, D.: ADM-Aeolus retrieval algorithms for aerosol and cloud products, Tellus A, 60, 273–288, https://doi.org/10.1111/j.1600-0870.2007.00287.x, 2008.

Flament, T., Trapon, D., Lacour, A., Dabas, A., Ehlers, F., and Huber, D.: Aeolus L2A aerosol optical properties product: standard correct algorithm and Mie correct algorithm, Atmos. Meas. Tech., 14, 7851–7871, https://doi.org/10.5194/amt-14-7851-2021, 2021.

Flesia, C. and Korb, C. L.: Theory of the double-edge molecular technique for Doppler lidar wind measurement, Appl. Opt., 38, 432–440, https://doi.org/10.1364/AO.38.000432, 1999.

Garnier, A. and Chanin, M. L.: Description of a Doppler rayleigh LIDAR for measuring winds in the middle atmosphere, Appl. Phys. B, 55, 35–40, 10.1007/BF00348610, 1992.

Garnier, A., Pelon, J., Vaughan, M. A., Winker, D. M., Trepte, C. R., and Dubuisson, P.: Lidar multiple scattering factors inferred from CALIPSO lidar and IIR retrievals of semi-transparent cirrus cloud optical depths over oceans, Atmos. Meas. Tech., 8, 2759–2774, https://doi.org/10.5194/amt-8-2759-2015, 2015.

Gu, Z., Witschas, B., van de Water, W., and Ubachs, W.: Rayleigh–Brillouin scattering profiles of air at different temperatures and pressures, Appl. Opt., 52, 4640–4651, https://doi.org/10.1364/AO.52.004640, 2013.

Hair, J. W., Hostetler, C. A., Cook, A. L., Harper, D. B., Ferrare, R. A., Mack, T. L., Welch, W., Izquierdo, L. R., and Hovis, F. E.: Airborne High Spectral Resolution Lidar for profiling aerosol optical properties, Appl. Opt., 47, 6734–6752, https://doi.org/10.1364/AO.47.006734, 2008.

Hersbach, H., Bell, B., Berrisford, P., Biavati, G., Horányi, A., Muñoz Sabater, J., Nicolas, J., Peubey, C., Radu, R., Rozum, I., Schepers, D., Simmons, A., Soci, C., Dee, D., and Thépaut, J.-N.: ERA5 hourly data on pressure lev-

els from 1940 to present, Copernicus Climate Change Service (C3S) Climate Data Store (CDS), ECMWF [data set], https://doi.org/10.24381/cds.bd0915c6, 2023.

Hu, Y.: Depolarization ratio–effective lidar ratio relation: Theoretical basis for space lidar cloud phase discrimination, Geophys. Res. Lett., 34, L11812, https://doi.org/10.1029/2007GL029584, 2007.

Hunt, W. H., Winker, D. M., Vaughan, M. A., Powell, K. A., Lucker, P. L., and Weimer, C.: CALIPSO Lidar Description and Performance Assessment, J. Atmos. Ocean. Technol., 26, 1214–1228, https://doi.org/10.1175/2009JTECHA1223.1, 2009.

Illingworth, A. J., Barker, H. W., Beljaars, A., Ceccaldi, M., Chepfer, H., Clerbaux, N., Cole, J., Delanoë, J., Domenech, C., Donovan, D. P., Fukuda, S., Hirakata, M., Hogan, R. J., Huenerbein, A., Kollias, P., Kubota, T., Nakajima, T., Nakajima, T. Y., Nishizawa, T., Ohno, Y., Okamoto, H., Oki, R., Sato, K., Satoh, M., Shephard, M. W., Velázquez-Blázquez, A., Wandinger, U., Wehr, T., and van Zadelhoff, G.: The EarthCARE Satellite: The Next Step Forward in Global Measurements of Clouds, Aerosols, Precipitation, and Radiation, B. Am. Meteorol. Soc., 96, 1311–1332 https://doi.org/10.1175/BAMS-D-12-00227.1, 2015.

IPCC: Climate Change 2013: The Physical Science Basis, Cambridge University Press, 1535 pp., https://doi.org/10.1017/CBO9781107415324, 2014.

IPCC: Annex I: Observational products. Climate Change 2021: The Physical Science Basis, edited by: Masson-Delmotte, V., Zhai, P., Pirani, A., Connors, S. L., Péan, C., Berger, S., Caud, N., Chen, Y., Goldfarb, L., Gomis, M. I., Huang, M., Leitzell, K., Lonnoy, E., Matthews, J. B. R., Maycock, T. K., Waterfield, T., Yelekçi, O., Yu, R., and Zhou, B., Cambridge University Press, 2061–2085, https://doi.org/10.1017/9781009157896.015, 2021.

Kar, J., Vaughan, M. A., Lee, K.-P., Tackett, J. L., Avery, M. A., Garnier, A., Getzewich, B. J., Hunt, W. H., Josset, D., Liu, Z., Lucker, P. L., Magill, B., Omar, A. H., Pelon, J., Rogers, R. R., Toth, T. D., Trepte, C. R., Vernier, J.-P., Winker, D. M., and Young, S. A.: CALIPSO lidar calibration at 532 nm: version 4 nighttime algorithm, Atmos. Meas. Tech., 11, 1459–1479, https://doi.org/10.5194/amt-11-1459-2018, 2018.

Ke, J., Sun, Y., Dong, C., Zhang, X., Wang, Z., Lyu, L., Zhu, W., Ansmann, A., Su, L., Bu, L., Xiao, D., Wang, S., Chen, S., Liu, J., Chen, W., and Liu, D.: Development of China's first space-borne aerosol-cloud high-spectral-resolution lidar: retrieval algorithm and airborne demonstration, PhotoniX, 3, 17, https://doi.org/10.1186/s43074-022-00063-3, 2022.

King, M. D., Kaufman, Y. J., Tanré, D., and Nakajima, T.: Remote Sensing of Tropospheric Aerosols from Space: Past, Present, and Future, B. Am. Meteorol. Soc., 80, 2229–2260, https://doi.org/10.1175/1520-0477(1999)080<2229:RSOTAF>2.0.CO;2, 1999.

Legras, B., Duchamp, C., Sellitto, P., Podglajen, A., Carboni, E., Siddans, R., Grooß, J.-U., Khaykin, S., and Ploeger, F.: The evolution and dynamics of the Hunga Tonga–Hunga Ha'apai sulfate aerosol plume in the stratosphere, Atmos. Chem. Phys., 22, 14957–14970, https://doi.org/10.5194/acp-22-14957-2022, 2022.

Levy, R. C., Mattoo, S., Munchak, L. A., Remer, L. A., Sayer, A. M., Patadia, F., and Hsu, N. C.: The Collection 6 MODIS aerosol products over land and ocean, Atmos. Meas. Tech., 6, 2989–3034, https://doi.org/10.5194/amt-6-2989-2013, 2013.

Li, Z., Liu, Z., Yan, Z., and Guo, J.: Research on characters of the marine atmospheric boundary layer structure and aerosol profiles by high spectral resolution lidar, Opt. Eng., 47, 086001, https://doi.org/10.1117/1.2969122, 2008.

Liu, D., Yang, Y., Cheng, Z., Huang, H., Zhang, B., Ling, T., and Shen, Y.: Retrieval and analysis of a polarized high-spectral-resolution lidar for profiling aerosol optical properties, Opt. Express, 21, 13084–13093, 10.1364/OE.21.013084, 2013.

Liu, D., Zheng, Z., Chen, W., Wang, Z., Li, W., Ke, J., Zhang, Y., Chen, S., Cheng, C., and Wang, S.: Performance estimation of space-borne high-spectral-resolution lidar for cloud and aerosol optical properties at 532 nm, Opt. Express, 27, A481–A494, https://doi.org/10.1364/OE.27.00A481, 2019.

Liu, Z. S., Chen, W. B., Zhang, T. L., Hair, J. W., and She, C. Y.: An incoherent Doppler lidar for ground-based atmospheric wind profiling, Appl. Phys. B, 64, 561–566, https://doi.org/10.1007/s003400050215, 1997.

Lohmar, F. J.: World geodetic system 1984 – geodetic reference system of GPS orbits, Berlin, Heidelberg, 1988, 476–486, https://doi.org/10.1007/BFb0011360, 1988.

Luthcke, S. B., Thomas, T. C., Pennington, T. A., Rebold, T. W., Nicholas, J. B., Rowlands, D. D., Gardner, A. S., and Bae, S.: ICESat-2 Pointing Calibration and Geolocation Performance, Earth Space Sci., 8, e2020EA001494, https://doi.org/10.1029/2020EA001494, 2021.

Matthew, J. M. and James, D. S.: Comparison of two direct-detection Doppler lidar techniques, Opt. Eng., 37, 2675–2686, https://doi.org/10.1117/1.601804, 1998.

Müller, D., Hostetler, C. A., Ferrare, R. A., Burton, S. P., Chemyakin, E., Kolgotin, A., Hair, J. W., Cook, A. L., Harper, D. B., Rogers, R. R., Hare, R. W., Cleckner, C. S., Obland, M. D., Tomlinson, J., Berg, L. K., and Schmid, B.: Airborne Multiwavelength High Spectral Resolution Lidar (HSRL-2) observations during TCAP 2012: vertical profiles of optical and microphysical properties of a smoke/urban haze plume over the northeastern coast of the US, Atmos. Meas. Tech., 7, 3487–3496, https://doi.org/10.5194/amt-7-3487-2014, 2014.

Pan, H., Huang, J., Kumar, K. R., An, L., and Zhang, J.: The CALIPSO retrieved spatiotemporal and vertical distributions of AOD and extinction coefficient for different aerosol types during 2007–2019: A recent perspective over global and regional scales, Atmos. Environ., 274, 118986, https://doi.org/10.1016/j.atmosenv.2022.118986, 2022.

Sayer, A. M., Smirnov, A., Hsu, N. C., and Holben, B. N.: A pure marine aerosol model, for use in remote sensing applications, J. Geophys. Res.-Atmos., 117, D05213, https://doi.org/10.1029/2011JD016689, 2012.

Schuster, G. L., Vaughan, M., MacDonnell, D., Su, W., Winker, D., Dubovik, O., Lapyonok, T., and Trepte, C.: Comparison of CALIPSO aerosol optical depth retrievals to AERONET measurements, and a climatology for the lidar ratio of dust, Atmos. Chem. Phys., 12, 7431–7452, https://doi.org/10.5194/acp-12-7431-2012, 2012.

She, C. Y., Alvarez, R. J., Caldwell, L. M., and Krueger, D. A.: High-spectral-resolution Rayleigh–Mie lidar measurement of aerosol and atmospheric profiles, Opt. Lett., 17, 541–543, https://doi.org/10.1364/OL.17.000541, 1992.

Shimizu, H., Lee, S. A., and She, C. Y.: High spectral resolution lidar system with atomic blocking filters for mea-

suring atmospheric parameters, Appl. Opt., 22, 1373–1381, https://doi.org/10.1364/AO.22.001373, 1983.

Shneider, M. N., Miles, R. B., and Pan, X.: Coherent Rayleigh-Brillouin scattering in molecular gases, Phys. Rev. A, 69, 33814, https://doi.org/10.1103/PhysRevA.69.033814, 2004.

Tenti, G., Boley, C. D., and Desai, R. C.: On the Kinetic Model Description of Rayleigh–Brillouin Scattering from Molecular Gases, Can. J. Phys., 52, 285–290, https://doi.org/10.1139/p74-041, 1974.

Vaughan, M., Garnier, A., Josset, D., Avery, M., Lee, K.-P., Liu, Z., Hunt, W., Pelon, J., Hu, Y., Burton, S., Hair, J., Tackett, J. L., Getzewich, B., Kar, J., and Rodier, S.: CALIPSO lidar calibration at 1064 nm: version 4 algorithm, Atmos. Meas. Tech., 12, 51–82, https://doi.org/10.5194/amt-12-51-2019, 2019.

Wandinger, U., Haarig, M., Baars, H., Donovan, D., and van Zadelhoff, G.-J.: Cloud top heights and aerosol layer properties from EarthCARE lidar observations: the A-CTH and A-ALD products, Atmos. Meas. Tech., 16, 4031–4052, https://doi.org/10.5194/amt-16-4031-2023, 2023.

Wang, Q., Bu, L., Tian, L., Xu, J., Zhu, S., and Liu, J.: Validation of an airborne high spectral resolution Lidar and its measurement for aerosol optical properties over Qinhuangdao, China, Opt. Express, 28, 24471–24488, https://doi.org/10.1364/OE.397582, 2020.

Wehr, T., Kubota, T., Tzeremes, G., Wallace, K., Nakatsuka, H., Ohno, Y., Koopman, R., Rusli, S., Kikuchi, M., Eisinger, M., Tanaka, T., Taga, M., Deghaye, P., Tomita, E., and Bernaerts, D.: The EarthCARE mission – science and system overview, Atmos. Meas. Tech., 16, 3581–3608, https://doi.org/10.5194/amt-16-3581-2023, 2023.

Winker, D. M., Hunt, W. H., and McGill, M. J.: Initial performance assessment of CALIOP, Geophys. Res. Lett., 34, L19803, https://doi.org/10.1029/2007GL030135, 2007.

Winker, D. M., Vaughan, M. A., Omar, A., Hu, Y., Powell, K. A., Liu, Z., Hunt, W. H., and Young, S. A.: Overview of the CALIPSO Mission and CALIOP Data Processing Algorithms, J. Atmos. Ocean. Technol., 26, 2310–2323, https://doi.org/10.1175/2009JTECHA1281.1, 2009.

Young, S. A. and Vaughan, M. A.: The Retrieval of Profiles of Particulate Extinction from Cloud-Aerosol Lidar Infrared Pathfinder Satellite Observations (CALIPSO) Data: Algorithm Description, J. Atmos. Ocean. Technol., 26, 1105–1119, https://doi.org/10.1175/2008JTECHA1221.1, 2009.

Young, S. A., Vaughan, M. A., Garnier, A., Tackett, J. L., Lambeth, J. D., and Powell, K. A.: Extinction and optical depth retrievals for CALIPSO's Version 4 data release, Atmos. Meas. Tech., 11, 5701–5727, https://doi.org/10.5194/amt-11-5701-2018, 2018.

Yu, X., Chen, B., Min, M., Zhang, X., Yao, L., Zhao, Y., Wang, L., Wang, F., and Deng, X.: Simulating return signals of a spaceborne high-spectral resolution lidar channel at 532 nm, Opt. Commun., 417, 89–96, https://doi.org/10.1016/j.optcom.2018.02.046, 2018.

Zhang, Y., Liu, D., Zheng, Z., Liu, Z., Hu, D., Qi, B., Liu, C., Bi, L., Zhang, K., Wen, C., Jiang, L., Liu, Y., Ke, J., and Zang, Z.: Effects of auxiliary atmospheric state parameters on the aerosol optical properties retrieval errors of high-spectral-resolution lidar, Appl. Opt., 57, 2627–2637, https://doi.org/10.1364/AO.57.002627, 2018.